COMBINED STATIC-CYCLIC MULTI-AXIAL CRACK PROPAGATION IN CRUCIFORM SPECIMENS

Venanzio Giannella*, Guido Dhondt**, Christian Kontermann*** and Roberto Citarella****.

*) Dept. of Industrial Engineering, University of Salerno, via G. Paolo II, 132, Fisciano (SA), Italy; vgiannella@unisa.it
**) MTU Aero Engines AG, Dachauer Str. 665, 80995 Munich, Germany; guido.dhondt@mtu.de (corresponding author)
***) Chair and Institute for Materials Technology, TU Darmstadt, Grafenstr. 2, 64283 Darmstadt, Germany; kontermann@mpa-ifw.tu-darmstadt.de
****) Dept. of Industrial Engineering, University of Salerno, via G. Paolo II, 132, Fisciano (SA), Italy; rcitarella@unisa.it

Abstract: Two cracks, initiated from the opposite tips of a 45° inclined central notch, were considered in cruciform specimens made of Ti6246. A static load was applied along one arm of the specimen and a cyclic load (R=-1) was applied along the other arm. Crack propagation was carefully monitored by optical means for different ratios of static to cyclic load. The observed crack propagation was simulated using two numerical tools, involving two different mixed-mode crack propagation prediction methods. The experimental evidence shows that there is a switch in crack propagation direction from orthogonal to the cyclic load at low static load levels to orthogonal to the static load for high static load levels. Both numerical procedures were able to predict this switch, albeit at slightly different static to cyclic load ratios.

Keywords: Cruciform specimen, LCF, HCF, multi-axial, crack propagation direction

1. Introduction

Three-dimensional crack growth simulations have assumed increased relevance over the last few decades. Early work was focused on building the framework to appropriately represent cracks with complex geometries, and calculate the related Stress Intensity Factors (SIFs) along the crack front [1]. As crack propagation capabilities increased, much of the effort went into the development of the framework necessary to model the extending crack with minimal user workload, for instance by Finite Element Method (FEM) codes, such as FRANC3D [2], CRACKTRACER3D [3], ZENCRACK [4], and by Dual Boundary Element Method (DBEM) codes, such as BEASY [5]. As shown in recent works, these methods nowadays allow to perform automatic 3D fatigue crack growth simulations for cracks in large structures [6-7], in the presence of residual stresses generated by plastic deformations [8-12] and with allowance for load spectrum effects [13]. Additionally, hybrid FEM - DBEM global-local approaches have been proposed along the years [14-16]: these approaches take advantage of both the FEM versatility when modelling the global problem, and of the higher efficiency of DBEM for simulating crack-growth in restricted subdomains. An overall extended review on the numerical codes nowadays available for modelling fracture can be found in [17].

In the past, non-planar 3D crack growth algorithms typically utilized 2D mode I/II crack growth theories that worked well for a wide range of engineering applications. Traditional crack growth criteria, such as the Maximum Tangential Stress (MTS) criterion [18], assume proportional loading (K_{II}/K_I = constant during one cycle), and predict crack growth along a $K_{II} \approx 0$ path. Sih [19] proposed the Minimum Strain Energy Density criterion (MSED) to govern the direction of the crack for 2D mixed-mode situations. According to that criterion, the crack grows in the direction in which the strain energy density is minimum. Sih also extended the MSED criterion to 3D problems in [20]. Nevertheless, the criterion captures only the deflection angle θ and it is unable to predict the twist angle ψ. Therefore, it cannot predict non-planar fracture propagation in the presence of Mode-III loading, and it is difficult to apply the criterion when mixed-mode I/II/III fracture occurs. To overcome this limitation, Schöllmann [21]

proposed a Maximum Principal Stress (MPS) criterion by introducing an equivalent K-value based on the three basic fracture modes. It assumes that the crack will grow radially from the crack front and perpendicular to the maximum principal stress if such stress as soon as the latter reaches a critical value. Dhondt [22] uses a similar but not quite identical approach assuming that crack propagation takes place orthogonal to the largest principal stress of the asymptotic stress field. The method yields an equivalent K-factor and a value for θ and ψ along the crack front. Ayatollahi and Saboori [23] recently extended MTS and MSED criteria to general mixed-mode I/II/III fractures allowing to calculate both θ and ψ fracture angles numerically. Hussain et al. [24] proposed an Energy Release Rate (ERR) criterion to predict the direction and extension of crack growth in Mode-I and Mode-II states. They derived an ERR expression using a rigorous elasticity approach and use that expression to predict the direction and extension of crack growth.

Nevertheless, with the advance of the technology to model nonplanar cracks in complex geometries the problem of the crack path assessment has become more demanding, requiring propagation criteria that include HCF/LCF interaction, Mixed Non-Proportional Loading (MNPL), fracture mode asymmetry and both elastic and fracture resistance anisotropy. For non-proportional loading, the relative proportions of K_I, K_{II} and K_{III} vary with time throughout the cycle making the setup of effective crack path criteria more complicated. MNPL can result from any structural loading configuration wherein steady and cyclic loads are simultaneously acting along different directions, as for a turbine blade where the steady state centrifugal load (LCF) couples with the blade vibrations (HCF, Fig. 1).

In aero engines, the use of blisks (blade integrated disks) is state of the art in all compressor stages due to the significant weight savings compared to a configuration in which the blades are mounted in disk slots. Due to this type of design the question arises whether a crack in the blade initiated and propagating due to the HCF-loading (resonance vibrations during flight) may turn into the disk due to the centrifugal LCF-loading (which is nearly constant during a flight) and ultimately lead to a possibly catastrophic disk failure.

Cruciform specimens have been widely and successfully used in the last years to study propagating cracks undergoing multi-axial loading conditions [25-32]. This generally

allowed to determine carrying capacity of real damaged structural elements undergoing multiaxial loading conditions, or to look for patterns in the crack growth with variations of dominant parameters, such as loading biaxiality, temperature, material properties, etc. Nevertheless, few information was found in the literature to understand the crack growth directions of cracks in cruciform specimens subject to various ratios of static loads in one direction and dynamic loads in the second direction.

The basic idea beyond this work was to avoid the complex modelling of a blisk by means of the simpler modelling and testing of cruciform specimens (Fig. 1). To this aim, a crack was introduced under 45° in the cruciform specimens. The LCF loading was simulated by a static load along one arm of the cruciform, whereas the HCF loading was simulated by a cyclic load (at a frequency of 5 Hz) in a direction perpendicular to the static load. Tests were performed for different ratios of static to cyclic load. The resulting crack propagation direction and crack propagation rate were monitored and compared with predictions from FEM and DBEM.

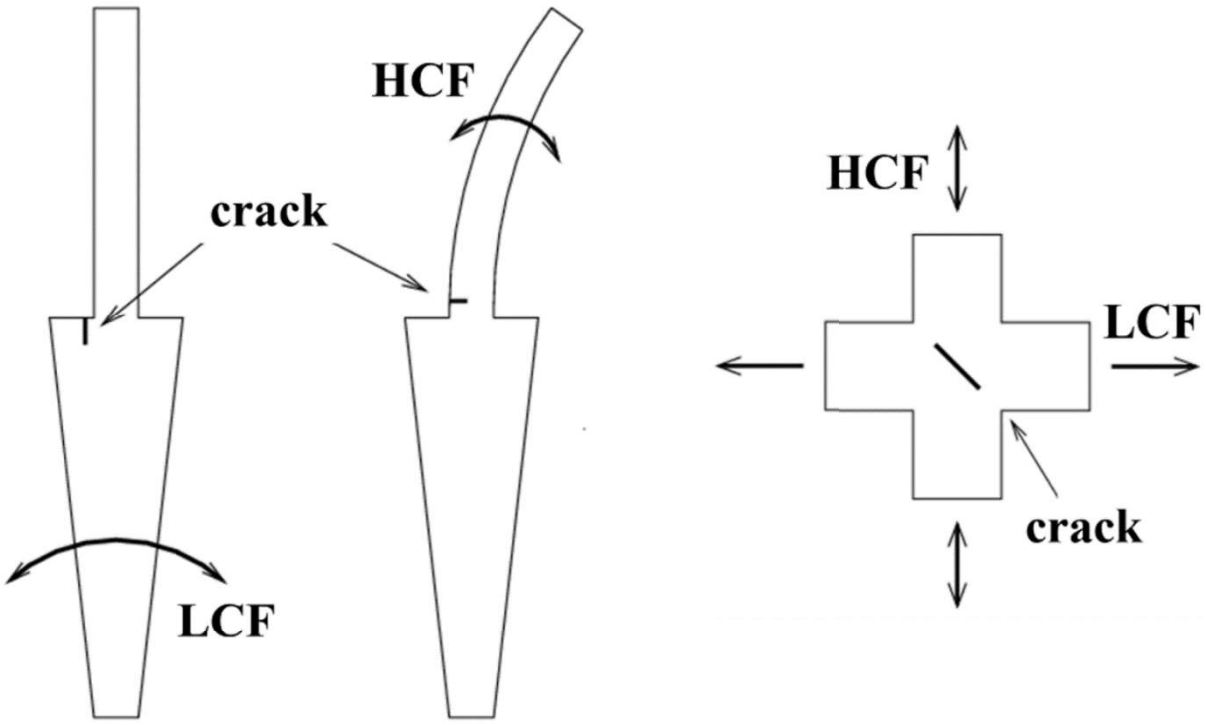

Figure 1: typical LCF and HCF loading in a blisk and corresponding cruciform specimen

In this context it is important to point to the assumptions made and the techniques used in the numerical simulations:

- Due to the rather low load level plasticity is limited to the crack tip, so K-based linear elastic fracture mechanics is used. No plastic stress intensity factor such as explained in [31] is needed.
- The crack propagation (size and direction) is solely based on the asymptotic stress field, i.e. based on $K_{I,}$ K_{II} and K_{III}. No T-stress [27] or critical distance concept [26] is used.
- Propagation is assumed to be driven by Mode-I, i.e. along a path for which $K_{II} \approx K_{III} \approx 0$.
- Crack propagation is calculated by applying an appropriate crack propagation law to the local K-values along the crack front. Therefore, no global crack propagation laws with constants based on the ratio of the loading along each arm of the cruciform specimen such as in [29] is derived.

The present article is organized as follows: at first the experimental set-up for the cruciform specimen tests is described. Subsequently, the algorithmic approach for the numerical calculation of multi-axial mixed-mode crack propagation used in CRACKTRACER3D (FEM) and BEASY (DBEM) is explained. Finally, the experimental tests are numerically simulated and the corresponding results are compared.

2. Experimental set-up

A biaxial testing machine with two servo-hydraulic actuators per axis was used to perform the cruciform tests [33]. The actuators are connected in a pairwise modal control scheme, so that the center of the specimen remains at the initial position during the whole test. All tests discussed in this paper have been performed under room temperature with load-controlled conditions for both axes. The cruciform specimen used [33-34] is manufactured out of slabs of the material Ti6246 and displayed in Figure 2 together with the crack starter notch. Within the test, the crack growth was monitored by both an Alternating Current Potential Drop (ACPD) measurement system

as well as a cycle synchronized optical camera system. After the tests the photographs were processed by using the DIC-software GOM-Correlate together with a self-written automatic crack detection tool based on the Dijkstra-Algorithm.

The crack starter notch was manufactured by means of electrical discharge machining with a specially manufactured electrode representing the negative form of the crack starter notch achieving notch radii in the range of 0.1 mm. The surface condition of the specimens has been produced by finely turning.

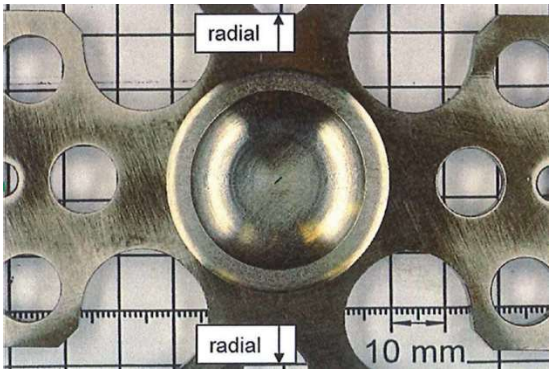

(a)

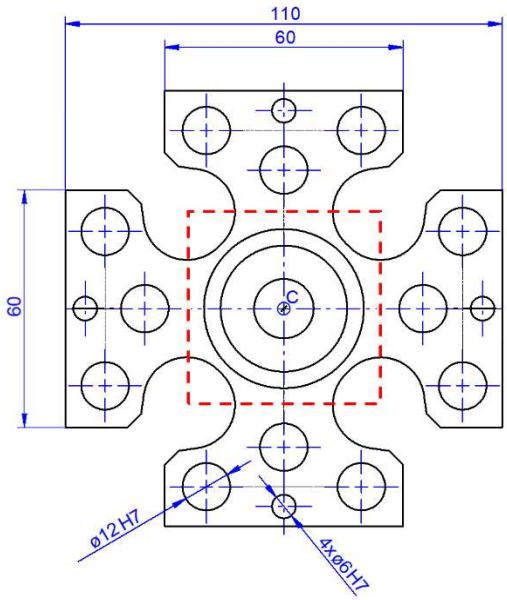

(b)

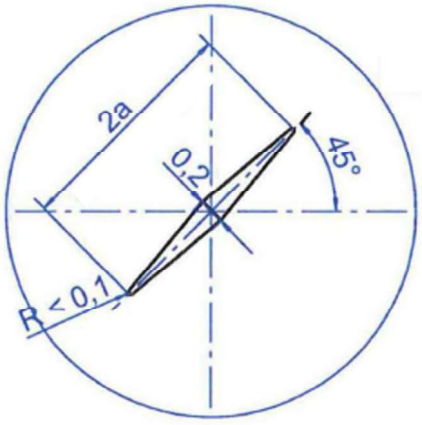

(c)

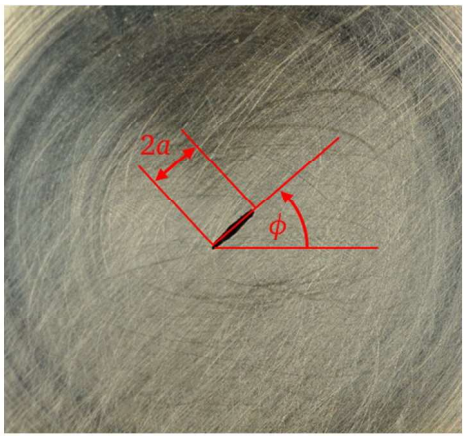

(d)

Figure 2: Geometric details of the cruciform specimen and of the crack starter notch

In this paper the results of the three tests outlined in Table 1 are discussed and theoretically re-evaluated.

Test No. (-)	Load step (-)	Static Load Force (kN)	Cyclic load		
			Force Amplitude (kN)	R-Ratio (-)	Frequency (Hz)
I	1	24.0	8.0	-1	5
II	1	2.0	16.0	-1	5
	2	12.0			
	3	24.0			
III	1	3.0	24.0	-1	5
	2	12.0			
	3	18.0			
	4	12.0			

Table 1: Test Matrix Overview.

The load in test I was chosen in such a way that the resulting stress level in the uncracked specimen is well within the linear elastic range (about 400 MPa) and that the ratio of the cyclic load to the static load is comparable to the ratio of the HCF loading to the LCF loading in a real blisk. Therefore, the K-concept is fully adequate to evaluate the crack propagation (small scale yielding at the crack tip) and no plastic analyses are necessary. Test II and III were triggered based on the experimental outcome of test I. This will be discussed in section 5.

For all specimens the angle ϕ as well as the total crack length $2a$ have been determined at both sides utilizing a measuring microscope. Here, values of $\phi = 44.2° \pm 0.8°$ for the crack angle and initial crack lengths of $2a = 1.97\ \mathrm{mm} \pm 0.13$

mm have been measured. The orientation of the crack was chosen such that no initial bias arises as to the direction of crack propagation w.r.t. the loading axes. The length of the initial crack is based on the experimental capabilities and the resulting K-values (not too small in order to get crack propagation and not too large such that enough life is left to get a large crack before failure).

For all tests, a pre-cracking procedure has been carried out in order to produce two initial cracks from the two notch tips. Only for the pre-cracking phases, cyclic loads with R=0.1 and f=5 Hz were applied to both cruciform axes and, starting from an initial load $F_{\max} = 8\,\mathrm{kN}$, loads were increased stepwise based on the fact whether a crack has been initiated or not. After successfully producing a crack with the potential to grow, the load was stepwise reduced to its initial value in order to let the crack grow out of the major part of the generated plastic zone.

3. Description of the FEM procedure

The numerical simulations were performed with the MTU software CRACKTRACER3D. It uses an iterative procedure to calculate the crack propagation of an arbitrary three-dimensional crack. Each iteration consists of an automatic meshing procedure for the structure with the actual crack (preprocessing step), a subsequent linear elastic finite element calculation and, finally, the determination of the K-values and a crack propagation increment (postprocessing step). In the preprocessing step part of the mesh for the uncracked structure (the so-called domain – it corresponds to the roughly square middle part in Fig. 3) is deleted and remeshed with a collapsed hexahedral mesh at the crack front and a tetrahedral mesh elsewhere. (Details in Fig. 4). The hexahedral mesh is a focused mesh with collapsed quarter-point elements at the crack tip able to generate the correct linear elastic $1/\sqrt{r}$ stress and strain singularity. In between the focused mesh at the crack tip and the mesh outside the domain tetrahedral elements are used out of flexibility reasons. The resulting meshes are connected using multiple point constraints. Any existing boundary conditions and loads are subsequently mapped from the uncracked mesh onto the cracked configuration. The purpose of the finite element calculation is the determination of the stresses at the

integration points ahead of the crack front, from which the K-factors are calculated. Next, the K_I, K_{II} and K_{III}-factors are converted into an equivalent K-factor K_{eq} and a propagation direction (characterized by the deflection angle θ) is calculated. This finally leads to a crack propagation increment by use of a modified Walker law, after which the whole procedure is started again. The calculation of the equivalent K-factor and the crack propagation direction are based on the largest principal value and the corresponding principal plane of the asymptotic stress field at the crack tip. This corresponds to the assumption that the crack propagates in mode-I. For details of the procedure the reader is referred to [34], for the modified Walker law [35] may be consulted.

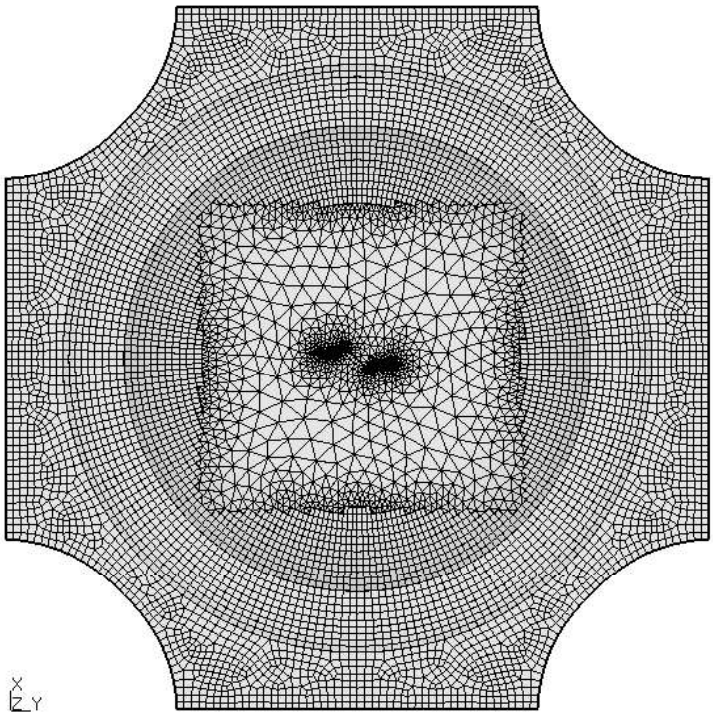

Figure 3: Cracked mesh for an intermediate crack propagation state of test I; the cyclic load is applied from left to right

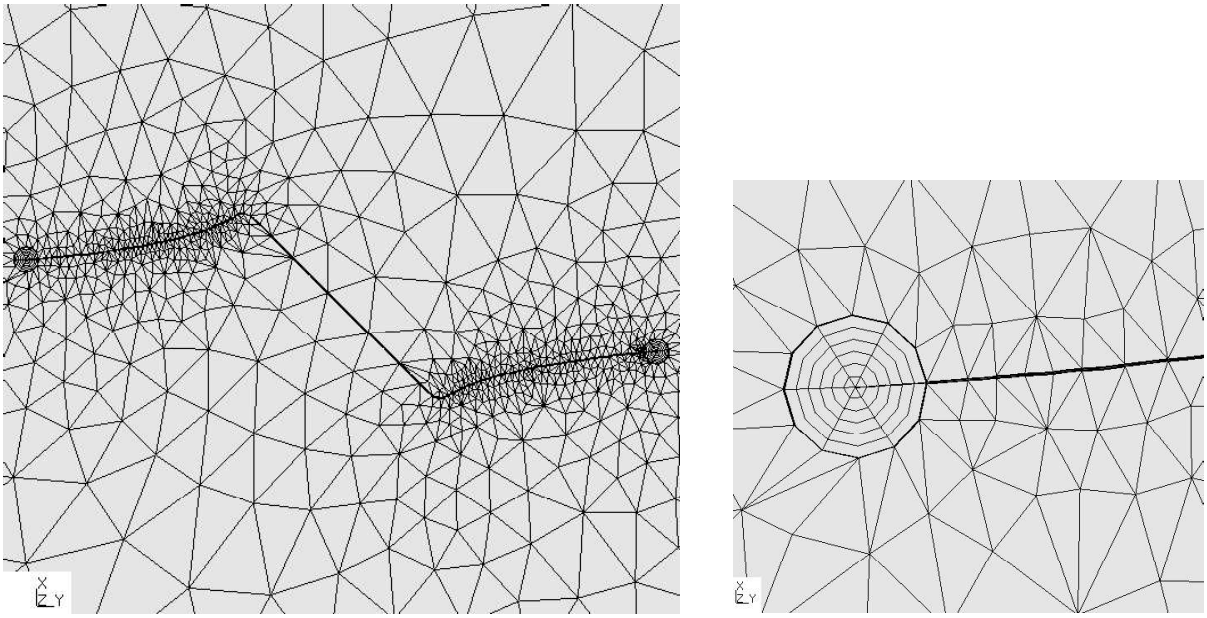

Figure 4: Mesh details in the crack vicinity (detailed view of the mesh in Fig. 3)

For the current calculations a mission was defined by three loading steps: the static (tensile) loading in x-direction, the static loading in x-direction plus the cyclic tensile loading in y-direction and the static loading in x-direction minus the cyclic tensile loading in y-direction (Figure 5). Each of these three loading steps leads to its own combination of K_I, K_{II} and K_{III} and consequently to possibly different values of K_{eq}, deflection angle θ and twist angle ψ. Therefore, a strategy is needed to determine the overall mission crack propagation increment based on the values in the individual steps.

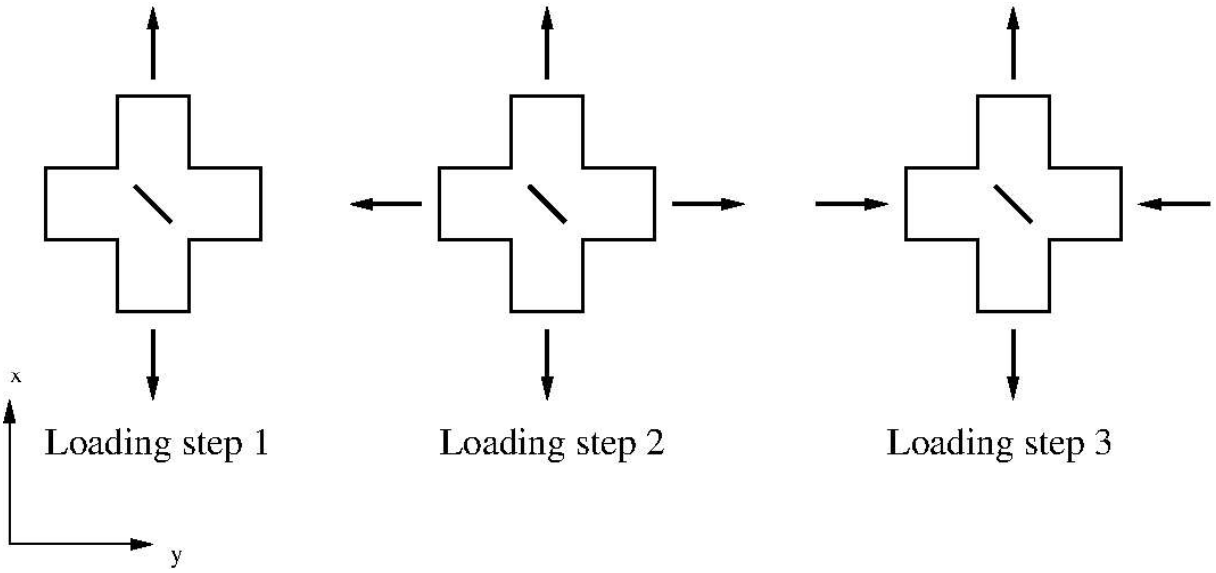

Figure 5: Loading steps in the mini-mission

In CRACKTRACER3D the mission deflection angle is defined as the deflection angle of the step (the so-called dominant step) which leads to the highest crack propagation rate obtained by substituting K_{eq} in a simple Paris-type crack propagation law. To this end, the values of K_{eq} in each step are determined based on K_I, K_{II} and K_{III} by looking for the largest principal stress of the asymptotic stress field [22]. They are subsequently substituted in a Paris-type crack propagation law in the form (cf. [35]):

$$\frac{da}{dN} = \left(\frac{da}{dN}\right)_{ref} \left(\frac{\max\left(K_{eq}, 0\right)}{\Delta K_{ref}(T)}\right)^{m(T)} , \tag{1}$$

where $\left(\frac{da}{dN}\right)_{ref}$ is usually chosen as 10^{-7} m/cycle, and $\Delta K_{ref}(T)$ and $m(T)$ are temperature-dependent material constants.

	static	static+cyclic	static-cyclic
K_I (MPa.m$^{0.5}$)	0.49	2.46	-1.47
K_{II} (MPa.m$^{0.5}$)	0.83	-2.48	4.14
K_{eq} (MPa.m$^{0.5}$)	1.25	4.42	4.03
θ (°)	-59.7	53.3	-77.4
da/dN (m/cycle)	2.99e-11	1.32e-9	9.99e-10

Table 2a: K-values and deflection angle for a static load of 2 kN

This procedure is illustrated in Tables 2a and 2b for a cyclic load of ±8 kN and a static load of 2 kN and 24 kN, respectively. The two individual K-values (K_{III} is not listed since it is zero), the resultant equivalent K-value, the deflection angle and the crack propagation rate according to Eq. (1) are shown for the three steps of the mini-mission consisting of static, static+cyclic and static-cyclic loading. One notices that step 2 is dominant for the low static loading while step 3 is dominant for the high static loading. Therefore, for the low static loading the mission deflection angle is taken from step 2 (53.3°), whereas for the high static loading it is taken from step 3 (-65.0°).

	static	static+cyclic	static-cyclic
K_I (MPa.m$^{0.5}$)	5.90	7.87	3.94
K_{II} (MPa.m$^{0.5}$)	9.93	6.62	13.24
K_{eq} (MPa.m$^{0.5}$)	15.00	12.75	17.54
θ (°)	-59.7	-50.3	-65.0
da/dN (m/cycle)	5.17e-8	3.17e-8	8.26e-8

Tabel 2b: K-values and deflection angle for a static load of 24 kN

Once the dominant step is determined the Keq-values in each loading step are re-evaluated (yielding $_{Keq,corr}$) based on this new information. Indeed, in Tables 2a,b K_{eq} is the highest principal asymptotic stress (normalized through multiplication by $\sqrt{r}$, see [3] for details; any further occurrence of the asymptotic stress in this article will be assumed to be normalized in the same way) in each loading step separately. Now, this is corrected into the principal asymptotic stress which acts in a principal plane as closely as possible to the principal plane corresponding to the highest principal asymptotic stress in the dominant step. This is verified by taking the scalar product of the normal to the planes. This can lead to the selection of a principal asymptotic stress in some loading steps which is not the highest for that loading step. In the present example this is the case for loading step 1 and loading step 3 for the 2 kN static load. This is illustrated in Table 3. For a static loading of 24 kN no change in principal planes took place and the corrected $K_{eq,corr}$ values are identical to the uncorrected ones.

	static	static+cyclic	static-cyclic
K_{eq}(MPa.m$^{0.5}$)	1.25	4.42	4.03
$K_{eq,corr}$(MPa.m$^{0.5}$)	0.43	4.42	-1.15

Table 3: Corrected equivalent K-values and deflection angles for a static load of 2 kN

At the present stage the procedure explained in the previous paragraphs has led to equivalent K-factors in each loading step separately and a mission deflection angle (one angle applicable to the whole mission). Next, cycle extraction is applied to obtain a mission crack propagation rate. To that effect a suitable one-dimensional function has to be identified. The da/dN values from Eq. (1) seem suitable, since they unite the effect of stress through K_{eq} and the effect of temperature through the material constants m and ΔK_{ref}. What is lost, however, is the sign of K_{eq}, leading to exclusively positive R-values for the extracted cycles. To remedy this a new crack propagation rate is calculated based on $K_{eq,corr}$ in each loading step separately according to

$$\frac{da}{dN} = \frac{K_{eq,corr}}{|K_{eq,corr}|}\left(\frac{da}{dN}\right)_{ref}\left(\frac{|K_{eq,corr}|}{\Delta K_{ref}(T)}\right)^{m(T)} , \quad (2)$$

Notice that the value of da/dN in Eq. (2) can be negative (if $K_{eq,corr}$ is negative). This ensures the extraction of cycles with negative R-values ($R=K_{eq,corr,min}/K_{eq,corr,max}$). Due to the correction of the K_{eq} values for the static load of 2 kN the corresponding da/dN values in Table 2a, which were used to determine the dominant loading step, are changed according to Eq. (2), leading to the values in Table 4 (notice the negative da/dN values for loading step 3). These are the values used for cycle extraction.

	static	static+cyclic	static-cyclic
(da/dN)-dominant	2.99e-11	1.32e-9	9.99e-10
(da/dN)-cycle extraction	1.18e-12	1.32e-9	-2.38e-11

Table 4: da/dN (m/cycle) curves for a static loading of 2kN used for determining the dominant step and for performing the cycle extraction

Since for a static loading of 24 kN the equivalent K-values were not changed and all of them are positive the da/dN values to which the cycle extraction is applied coincide with the ones used to determine the dominant step (Table 2b).

The cycle extraction is performed with the rainflow algorithm according to the method explained in [36]. Each cycle is characterized by $K_{eq,corr,min}$ and $K_{eq,corr,max}$. Let the temperature corresponding to $K_{eq,corr,max}$ be called T_{max} and similarly for the minimum equivalent K-factor. Then, the procedure in CRACKTRACER3D is such that the cycle is evaluated once at the temperature T_{max} and once at the temperature T_{min}. Subsequently, the highest crack propagation rate is taken.

4. Description of the DBEM procedure

Numerical simulations were also performed with the DBEM code BEASY [37]. The portion of the cruciform specimen circumscribed by the dashed (red) line in Fig. 2b, with related boundary conditions on the cutting surfaces, was considered as the reference model to be used in the DBEM environment.

The DBEM mesh shown in Fig. 6 comprises nearly 3900 linear boundary elements, rising up to 6000 elements for the last propagation steps (when larger cracks and finer meshes are required). The choice of using linear rather than quadratic elements is given by the fact that contacts between crack faces were considered (faster convergence was achieved).

The initial notch with two cracks, initiated at 45° at the two opposite tips after the precracking phase, was taken as the initial configuration for the simulations (Fig. 6b). The total length of the notch and cracks was 2 mm, corresponding to the specimen tested experimentally.

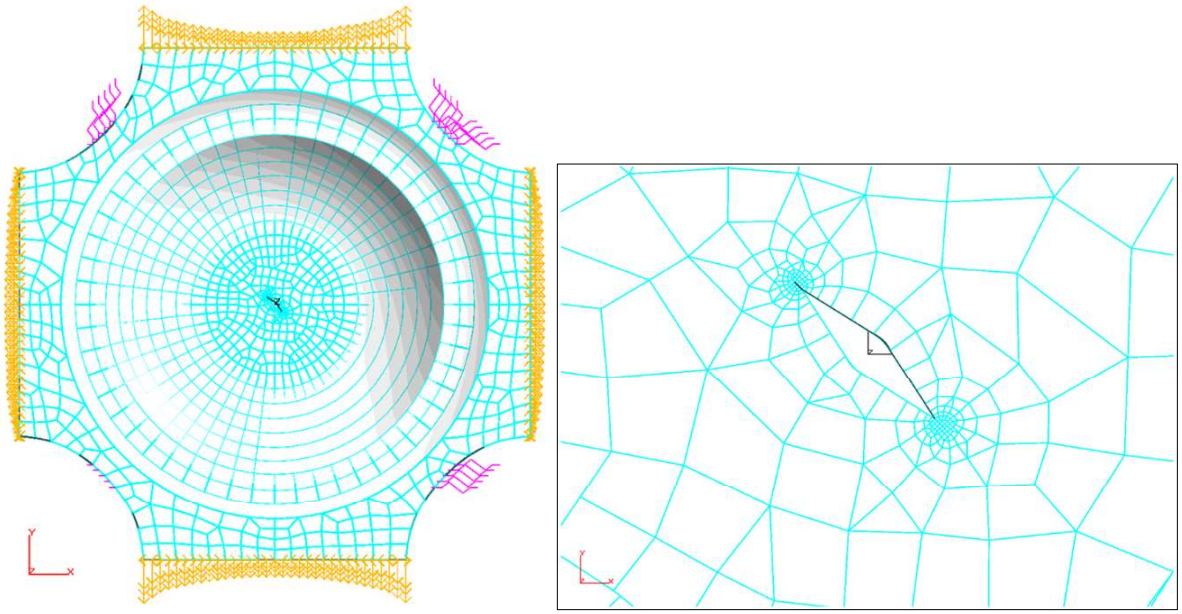

(a) (b)

Figure 6: DBEM model used for the numerical analyses (a) with highlight of the crack insertion area (b)

In order to be consistent with the FEM modelling of the experimental tests, preliminary FEM analyses were used to calculate the traction distributions on the DBEM cutting surfaces (those crossed by the dashed (red) line in Fig. 2b). A model like that shown in Fig 3 but without the crack was used for such a purpose. The FEM stresses evaluated on the cut surfaces were applied on the corresponding DBEM surfaces. In addition, springs of negligible stiffness were applied on few DBEM elements of the model in order to prevent rigid body motion. The final DBEM model with all loads applied is shown in Fig. 6a.

J-paths (rings of internal points) were introduced along the two crack fronts in order to compute the corresponding J-integral values. Such J distributions were then used to compute K_I, K_{II} and K_{III} values along the crack front by means of the procedure presented in [38-39].

The mission profile considered for the analyses was defined by means of two load cases:

1. a static tensile load in x-direction plus a cyclic tensile load in y-direction (load case A)
2. a static tensile load in x-direction plus a cyclic compressive load in y-direction (load case B).

Several criteria to determine K_{eq} by combining the three basic fracture modes have been proposed along the years, such as: Maximum principal [40], sum of squares [41] and Yaoming-Mi [42]. In particular, the Yaoming-Mi formula (Eq. (3)) was applied in this work to obtain an equivalent K_{eq} value for further use in the Walker crack growth law (Eq. (4)) [43]. A comparison among various formulations for calculating K_{eq} can be found in [44]. [5] provides a comparison between formulations for calculating deflection angles and crack growth rates, as well as for K_{eq}.

The stress ratio R considered in the Walker crack-growth law is calculated as in Eq. (5). Material fracture data are listed in Table 5. In particular, the Walker coefficient w was optimized in such a way that the classical Walker law used for the DBEM agreed with the modified Walker law used by MTU.

E [GPa]	υ [-]	C [mm/cycle/(MPa mm0.5)^m]]	m [-]	w [-]
120.4	0.32	4.83828E-13	3	0.67

Table 5: Main mechanical properties and Walker law parameters for Ti6246

The crack-growth angle θ_i was computed by means of the Minimum Strain Energy Density (MSED) criterion [19, 20] for each load case, i.e. load cases A and B. The criterion predicts the deflection angle of the crack for each load case θ_i by minimizing the strain energy density calculated as a function of the three basic K-values (Eq. (6)) [20]. No twist angle ψ can be calculated by means of MSED criterion [17]. Finally, the overall deflection angle θ was calculated by a weighted average of the single θ_i by means of Eq. (7), the weights of which are the K_{eq} values for each load case.

$$K_{eq} = \sqrt{\left(K_I + |K_{III}|\right)^2 + 2K_{II}^2} \tag{3}$$

$$\mathrm{da/dN} = \mathrm{C}\left[\Delta \mathrm{K}_{eq}/(1-\mathrm{R})^{1-\mathrm{w}}\right]^{\mathrm{m}} \tag{4}$$

$$R = K_{eq,min}/K_{eq,max} \tag{5}$$

$$S(\theta) = a_{11}(\theta)K_I^2 + a_{13}(\theta)K_I K_{II} + a_{22}(\theta)K_{II}^2 + a_{33}(\theta)K_{III}^2 \tag{6}$$

$$\theta = \frac{\theta^A|K_{eq}^A| + \theta^B|K_{eq}^B|}{|K_{eq}^A| + |K_{eq}^B|} \tag{7}$$

For some combinations of static and dynamic load magnitudes, load case 2 provided negative K_I values, with no physical meaning since it points to a mutual intersection of the crack faces. To circumvent this drawback, a nonlinear contact condition, with allowance for friction (friction coefficient f=0.3) was applied to the crack face elements for such load cases. In this way, the resulting K_I values became nearly null, the related K_{II} and K_{III} decreased due to friction effects, providing a direct impact on the K_{eq} values and eventually on the final growth angle θ (Eq. 7).

5. Comparison of the numerical and test results for the cruciform specimens

5.1. Numerical and experimental results for test I.

The first test (test I in Table 1) is characterized by a static loading of 24 kN and a dynamic loading of ±8 kN. The experimental crack paths are shown in Fig. 7a, whereas the numerical crack paths provided by CRACKTRACER3D and BEASY are visualized in Figures 7b and 7c, respectively. Please note that in order to simplify the comparison between the numerical and experimental results all figures in this section are oriented such that the static load is applied from the lower left to the upper right of the figure, whereas the cyclic load is applied from the upper left to the lower right.

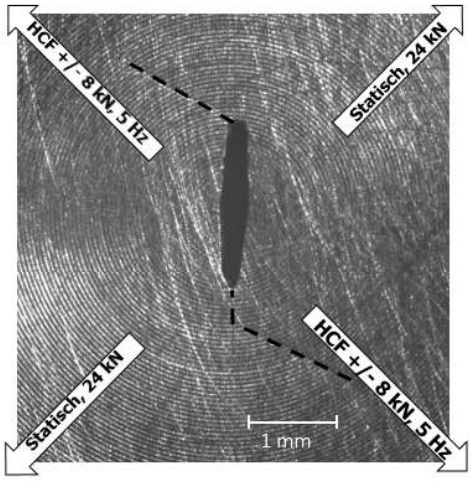

Figure 7a: Experimental test result of Test I

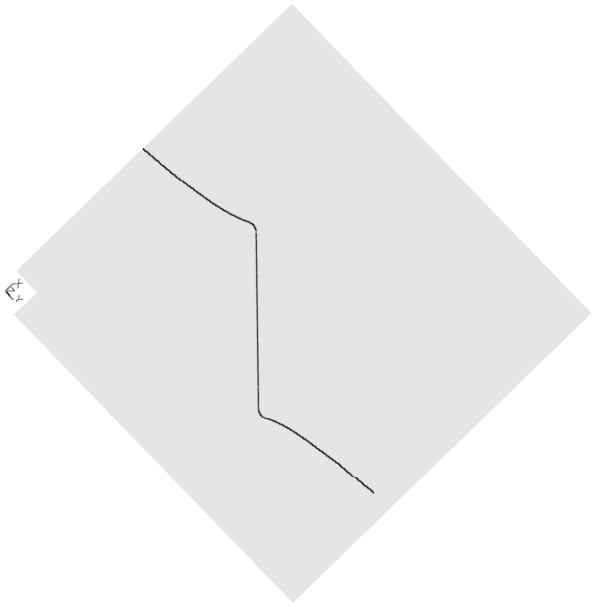

Figure 7b: FEM numerical crack propagation for Test I

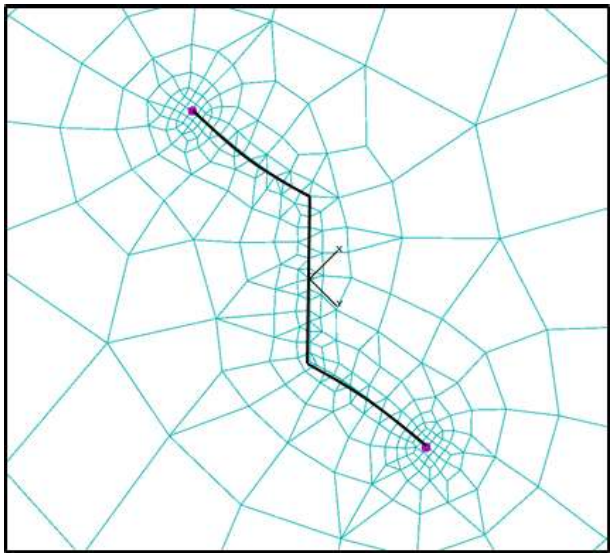

Figure 7c: DBEM numerical crack propagation for Test I.

In this test the crack propagation takes place in a direction orthogonal to the static load. This is confirmed by the numerical simulations both in CRACKTRACER3D and BEASY. Since the crack is open during the complete loading cycle no contact formulation in between the crack faces was needed. Not only the shape of the crack but also the crack length vs. the number of cycles is well reproduced by the two numerical approaches. This is shown in Figure 8, where “Size a” and “Size b” refer to measurements on the upper and lower surface of the cruciform specimen.

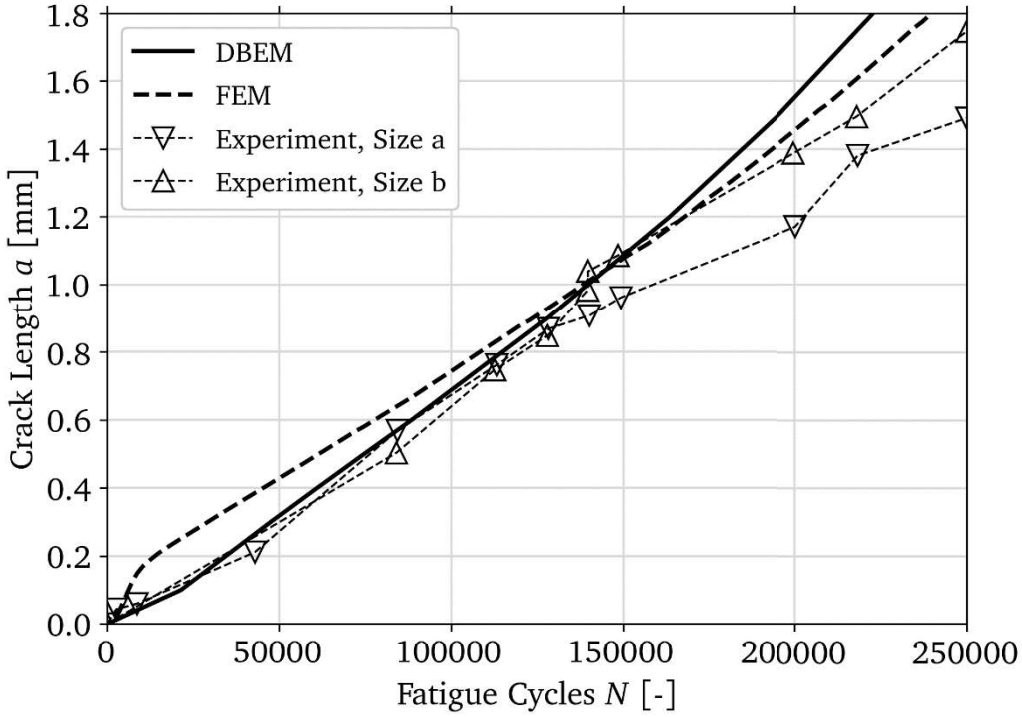

Figure 8: Crack length versus number of cycles for test I.

In summary, for this case (Test I in Table 1) it is possible to assess that:

- the calculation of the equivalent K-factor in combination with a classical crack propagation law calibrated by mode-I test data yields a correct crack propagation prediction
- the procedures for the propagation angle calculations turn out to be correct.

Transferring the results of test I to the blisk case, it means that a crack originating in the blade of a blisk due to vibrational loading (HCF) may in principal well turn into the disk and lead to a catastrophic failure due to the centrifugal loading (LCF). Therefore, each newly designed blisk has to be the subject of intensive investigations checking whether for this concrete blisk cracks starting in the blade may turn into the disk.

Now, it is clear that in the absence of static loading the crack propagation direction should be orthogonal to the cyclic loading. This means that a transition of the crack propagation direction from orthogonal to the cyclic loading to orthogonal to the static loading must take place for a static load in between 0 kN and 24 kN (always

considering a cyclic load of ±8 kN). In order to assess the value of such a transition static load, further experimental and numerical tests were performed. This was out of scientific interest rather than to answer questions from the engineering design department.

5.2. Experimental results for tests II and III (Table1)

Test II was scheduled with a static load much smaller than the cyclic load. In order to avoid problems with potential residual stresses the cyclic load was increased compared to test I to ±16 kN and a static load of 2 kN was applied (test II). Crack propagation due to this loading only occurred at the top crack front (Fig. 9a) and was indifferent, i.e. not perpendicular to the static nor to the cyclic load but somewhere in between. This crack propagation pattern was deemed to be due to residual stresses. Therefore, the static force was increased in a new loading step to 12 kN in order to overcome the residual stresses. Under the latter loading a crack started from the lower front (Fig. 9b) and grew orthogonal to the static load, whereas the crack at the upper front continued to grow indifferently. Since scaling should not alter the crack path, this test shows that the application of 6 ±8 kN leads to crack propagation orthogonal to the static load at least at the lower front. Further increasing the static load to 24 kN led to crack growth orthogonal to the static load at both crack fronts (Fig. 9c).

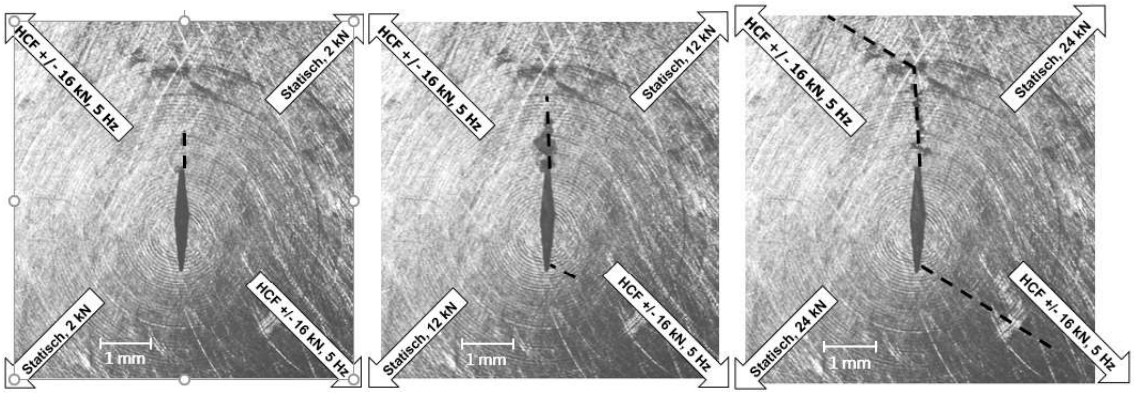

(a) (b) (c)

Figure 9 Experimental results for test II

In order to further investigate the range of low static loads and overcome any potential residual stresses the static and cyclic load were increased in test III to 3 kN and ±24 kN, respectively. The experimental result is shown in Fig. 10a. At the bottom front the crack grows indifferently, whereas at the top front it propagates after some indifferent crack growth orthogonal to the cyclic load. Increasing the static load to 12 kN in the next load step does not change this pattern (Fig. 10b). A further increase to 18 kN leads to bifurcation with secondary cracks propagating orthogonal to the static load (Fig 10c). Reducing the static load again to 12 kN leads to propagation of the cracks which were created before the bifurcation (Figs. 10d-e). This seems to indicate that the cracks grow orthogonal to the cyclic load for a static load below 4 kN and orthogonal to the static load for a static load above 6 kN (all loads scaled for a cyclic load of ±8 kN).

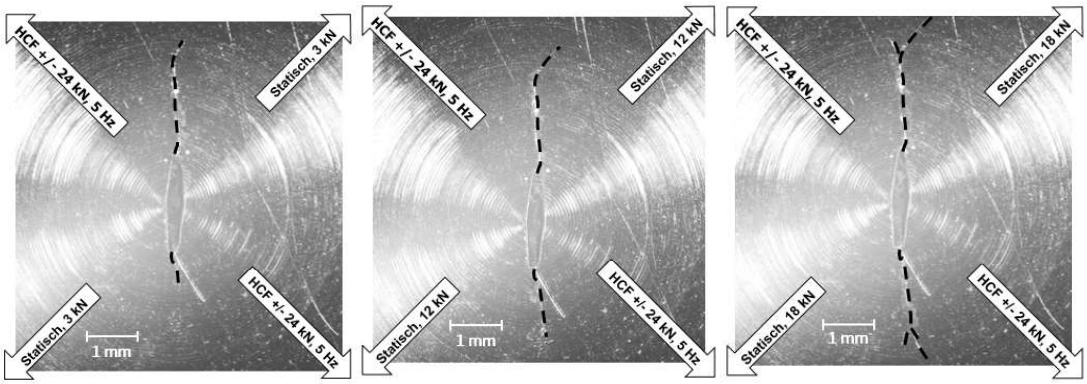

(a) (b) (c)

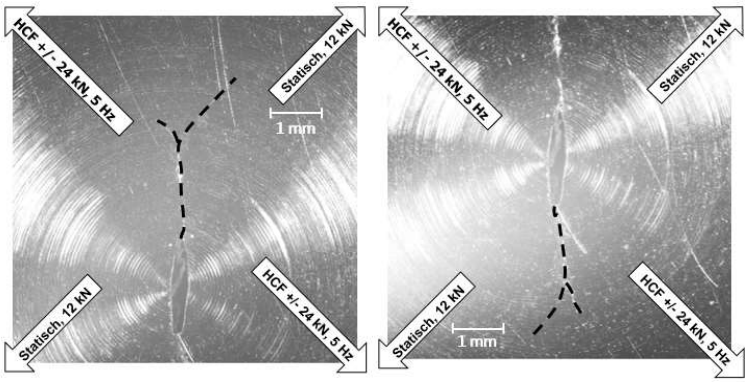

(d) (e)

Figures 10: Experimental results for test III.

5.3 FEM and DBEM results for various static to cyclic load ratios

Although this experimental outcome is highly complex (bifurcation, indeterminate crack propagation maybe due to residual stresses) an attempt was made to verify the simplified message formulated in the preceding paragraph by use of numerical methods. First, numerical simulations were performed with CRACKTRACER3D for values of the static load varying between 0 kN and 24 kN and a cyclic load of ±8 kN. It was found that below 2 kN the propagation was orthogonal to the cyclic load. Above 2.5 kN it was orthogonal to the static load. In between it was indeterminate (Fig. 11a-c; the cyclic load is applied from upper left to lower right). The change in direction was accompanied by a change in dominant loading step: below the shift the static load plus the cyclic load step was dominant, above the shift the static load minus the cyclic load step was dominant. Notice that Figure 11a is the superposition for the propagation at 0 kN and 2 kN static load, whereas Figure 11c is the superposition for the propagation at 2.5 kN, 3 kN, 4 kN, 5 kN, 10 kN, 15 kN, 20 kN and 24 kN. Therefore, these pictures are slightly blurred.

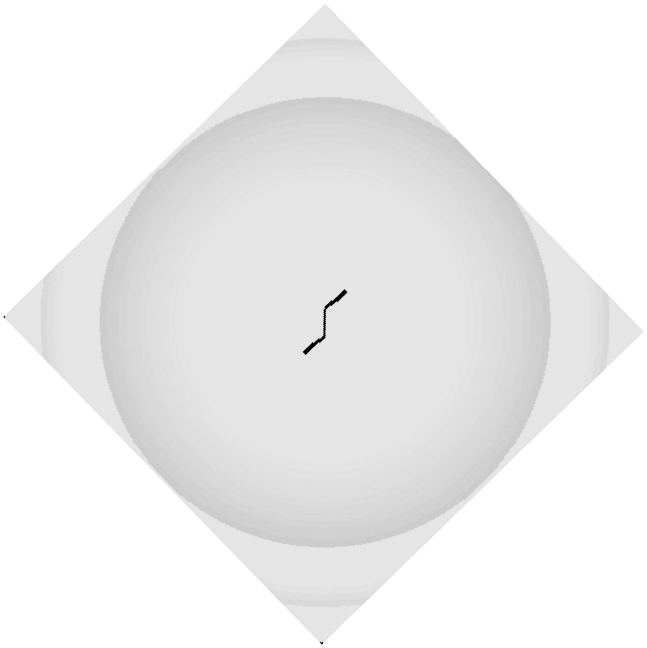

Fig 11a

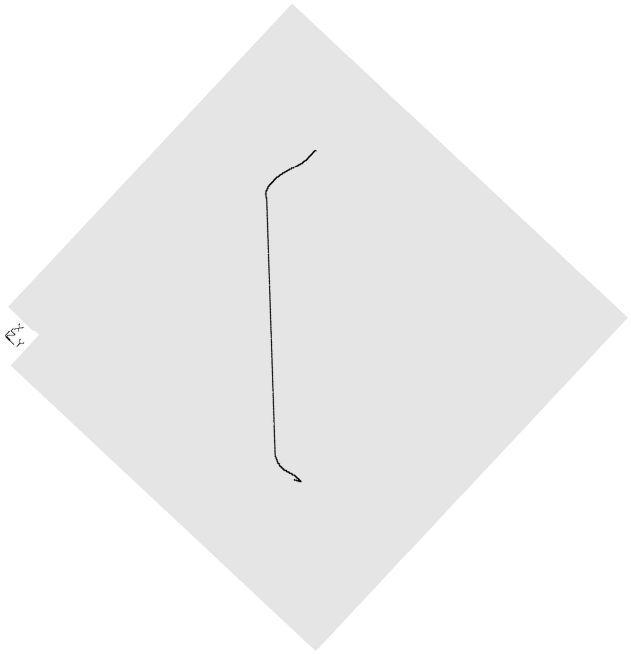

Fig 11b

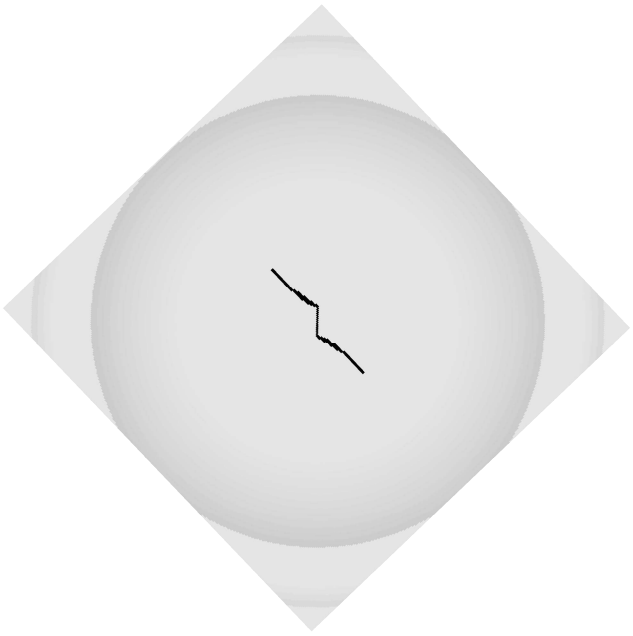

Figure 11c

Figure 11: Crack propagation due to a static load below 2kN (a), at 2.25 kN (b, zoomed-in view) and above 2.5 kN (c); the cyclic load is applied from upper left to lower right

Similar calculations were performed with BEASY. The results are summarized in Figure 12. The cyclic load was again set to ±8 kN and various crack-growth simulations were performed for various levels of the static load. It was found that the cracks propagate orthogonal to the static load when the latter has a magnitude higher than 2kN, whereas the cracks propagate parallel to the static load when such load has a nearly null magnitude. Figure 12 shows also the crack paths predicted with a 0 kN ± 8 kN and 0 kN + 8 kN (i.e. cyclic load replaced by a tensile static load) load. As expected, the 0 kN + 8 kN loading leads to propagation perpendicular to the cyclic load. Adding also the contribution of the negative part of the cyclic load (thus applying 0 kN ± 8 kN) leads to a smoother crack deflection but still perpendicular to the cyclic load.

It is worth noting that these simulations have been performed with contact between the crack surfaces. This required the explicit modelling of the initial notch in order to prevent an unrealistic contact between the notch surfaces.

The transition from propagation perpendicular to the cyclic load to perpendicular to the static load occurs when the static load is very small compared to the cyclic load amplitude. Such a transition occurs with the DBEM at a static load of about 1 kN which is significantly smaller than the transition value of 2.25 kN computed by CRACKTRACER3D and the estimated transition value of nearly 5 kN in the tests.

An explanation for such a low value for the transition load provided by the DBEM simulations can be related to the contact conditions between the crack faces. Indeed, Tables 2a and 2b show that the transition at increasing static load takes place as soon as the static-cyclic loading case becomes dominant in terms of K_{eq} w.r.t. the static+cyclic load case. Figures 13a and 13c show that contact takes place for the static+cyclic load case. The accompanying friction reduces the corresponding K_{eq}-values. For the static-cyclic load case contact is less relevant (Figure 13b and 13d), and no appreciable changes in K_{eq} are to be expected for such load cases. Therefore, the higher the friction between the crack faces is, the lower the transition load will be.

.

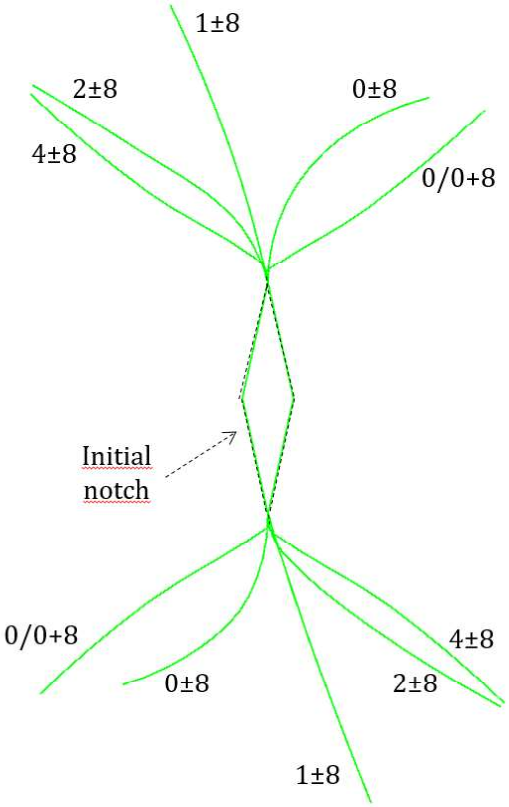

Figure 12: Crack propagation direction due to different static loads. The cyclic load is applied from top left to bottom right

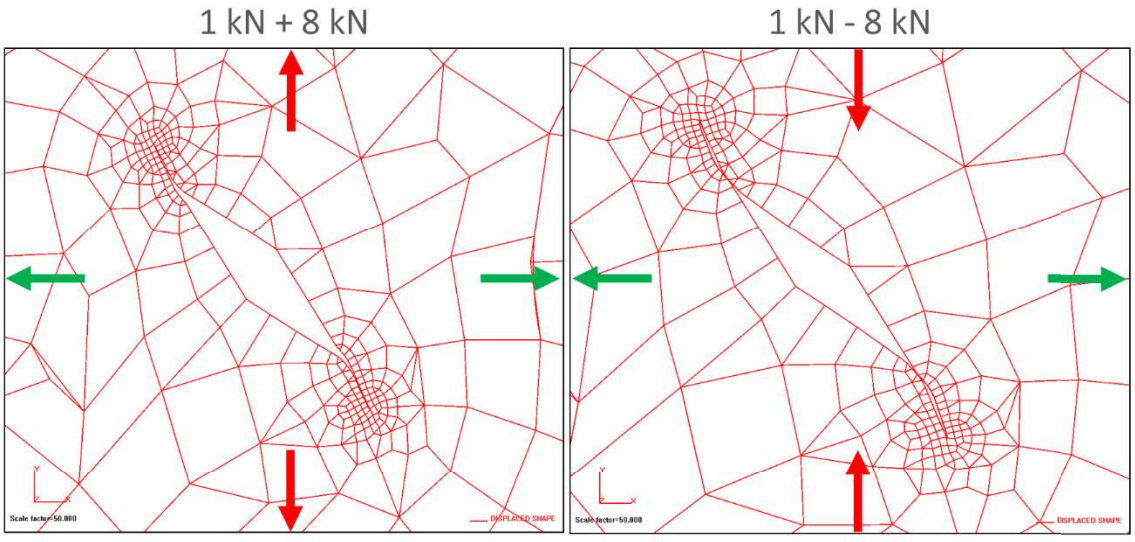

(a) (b)

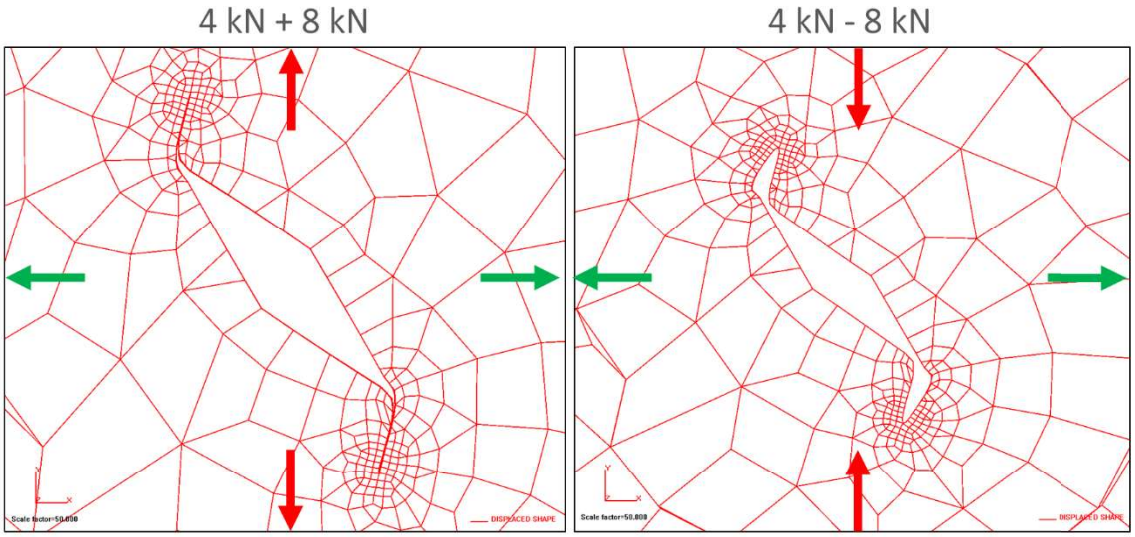

(c) (d)

Figure 13: DBEM deformed crack shape during the propagation for cyclic loads of ±8 kN (vertical arrows) and a static load of (a,b) 1 kN or (c,d) 4 kN.(horizontal arrows)

The prediction of the crack propagation vs. the number of cycles with CRACKTRACER3D is shown in Figure 14. For small static loads the crack propagation is relatively fast. Close to the transition load of 2.25 kN the propagation slows down considerably: for a 2.5 kN static load the number of cycles needed to reach a crack propagation of 0.4 mm is 3.5 times larger than for a static load of 2.25 kN. At this load the crack propagation direction changes from orthogonal to the cyclic load to orthogonal to the static load. For increasing static loads the propagation slowly accelerates to yield a crack propagation level similar to the case with zero static load.

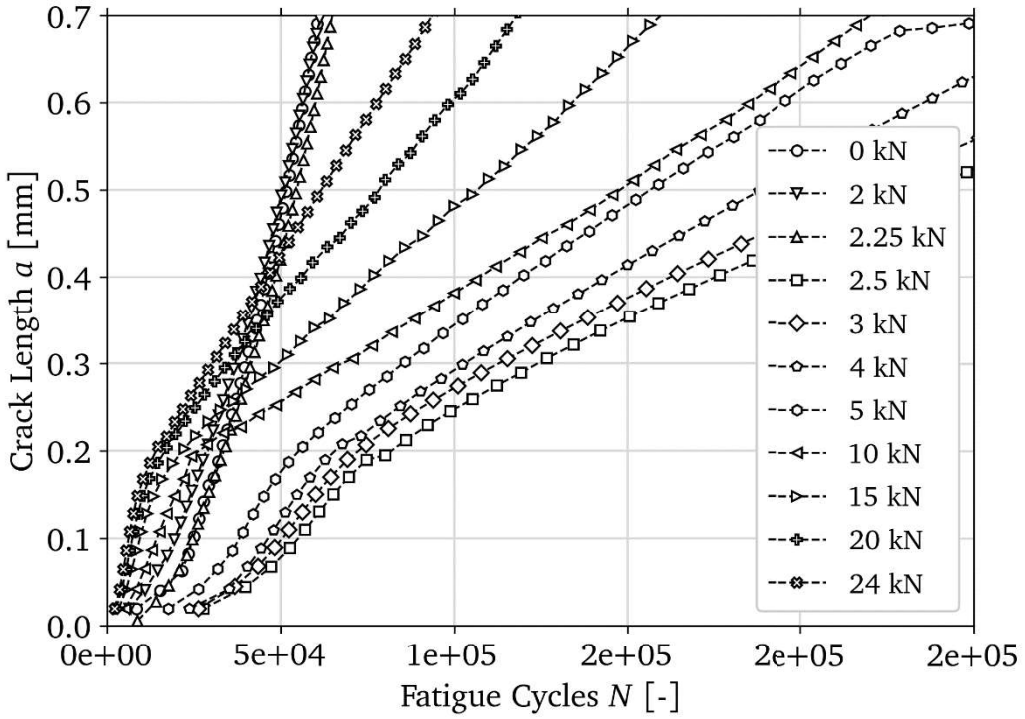

Fig. 14: Crack propagation for different static loads (CRACKTRACER3D)

A similar picture arises for the numerical analysis with the DBEM (Fig. 15). Without static load the crack propagation rate reaches a relatively high level. Slightly increasing the static load (transition region) the propagation drops down by a factor of two. With a further increase of the static load the crack propagation rate returns to levels corresponding to a zero static load. This means that adding a relatively small static load to the cyclic one produces a switch in the crack growth direction accompanied by a notable increase of the residual fatigue life.

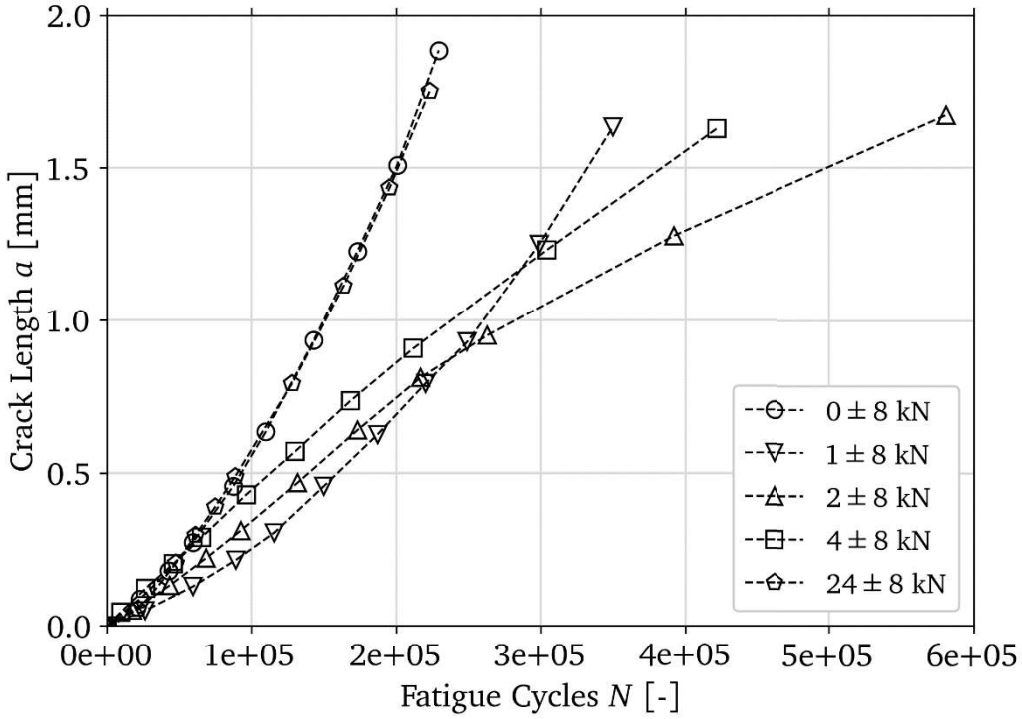

Fig. 15: DBEM crack propagation for different static loads

Conclusions

In order to investigate whether cracks initiated in the transition radius between blade and disk of a blisk and propagating due to HCF vibrational loading may turn into the disk driven by LCF centrifugal loading, cruciform specimen tests were set up subjected to a static loading in one direction and a cyclic loading in the other direction. At realistic ratios of cyclic to static loading the crack propagates orthogonal to the static loading, i.e. into the disk. This is confirmed quantitatively by the predictions of two different software programs, therefore adding to the credibility of the crack propagation criteria used in each of them. For smaller static to cyclic load ratios the crack propagation switches into a direction orthogonal to the cyclic loading. Although the test results are not easy to interpret due to bifurcation and residual stresses it looks as if the numerical codes underestimate the static to cyclic loading ratio of the switching point. Further experimental evidence and numerical calculations are deemed necessary to clarify this latter point.

This research did not receive any specific grant from funding agencies in the public, commercial, or non-for-profit sectors.

References

[1] Citarella, R., Buchholz, F.-G., Comparison of DBEM and FEM crack path predictions with experimental findings for a SEN-specimen under anti-plane shear loading, Key Engineering Materials 348-349 (2007) 129-132.

[2] Wawrzynek, P.A., Carter, B.J., Ingraffea, A.R., Advances in simulation of arbitrary 3d crack growth using FRANC3D/NG, In: Proceedings of the 12th international conference on fracture, Ottawa, June, (2009).

[3] Bremberg, D., Dhondt, G., Automatic 3-D crack propagation calculations: a pure hexahedral element approach versus a combined element approach, Int J Fract. 157 (2009) 109-118.

[4] Citarella, R., Lepore, M., Maligno, A., Shlyannikov, V., FEM simulation of a crack propagation in a round bar under combined tension and torsion fatigue loading, Frattura ed Integrità Strutturale, 31 (2015a) 138-147.

[5] Citarella, R., Giannella, V., Lepore, M., Dhondt, G., Dual boundary element method and finite element method for mixed-mode crack propagation simulations in a cracked hollow shaft, Fatigue Fract Eng Mater Struct., 41 (2018) 84-98.

[6] Citarella, R., Cricrì, G., Three-dimensional BEM and FEM submodelling in a cracked FML full scale aeronautic panel, Appl. Compos. Mater, 21(3) (2014) 557–577.

[7] Citarella, R., Lepore, M., Fellinger, J., Bykov, V., Schauer, F., Coupled FEM-DBEM method to assess crack growth in magnet system of Wendelstein 7-X, Fract. Struct. Integ, 26 (2013) 92–103.

[8] Citarella, R., Cricrì, G., Lepore, M., Perrella, M., Assessment of crack growth from a cold worked hole by coupled FEM-DBEM approach, Key Engineering

Materials, vols. 577–578, Trans Tech Publications, Switzerland, (2014) 669–672.

[9] Carlone, P., Citarella, R., Lepore, M., Palazzo, G.S., A FEM-DBEM investigation of the influence of process parameters on crack growth in aluminium friction stir welded butt joints, Int. J. Mater. Form, 8(4) (2015) 591–599.

[10] Citarella, R., Carlone, P., Lepore, M., Palazzo, G.S., Numerical–experimental crackgrowth analysis in AA2024-T3 FSWed butt joints, Adv. Eng. Softw., 80 (2015b) 47–57.

[11] Citarella, R., Carlone, P., Sepe, R., Lepore, M., DBEM crack propagation in frictionstir welded aluminum joints, Adv. Eng. Softw., 101 (2016a) 50-59.

[12] Citarella, R., Carlone, P., Lepore, M., Sepe, R., Hybrid technique to assess the fatigue performance of multiple cracked FSW joints, Eng. Fract. Mech., 162 (2016b) 38-50.

[13] Citarella, R., Cricrì, G., A two-parameter model for crack growth simulation by combined FEM-DBEM approach, Adv. Eng. Softw., 40(5) (2009) 363–377.

[14] Citarella, R., Giannella, V., Vivo, E., Mazzeo, M., FEM-DBEM approach for crack propagation in a low pressure aeroengine turbine vane segment, Theoretical and Applied Fracture Mechanics, 86(B) (2016c) 143-152.

[15] Giannella, V., Fellinger, J., Perrella, M., Citarella, R., Fatigue life assessment in lateral support element of a magnet for nuclear fusion experiment “Wendelstein 7-X”, Engineering Fracture Mechanics, 178 (2017a) 243-257.

[16] Giannella, V., Perrella, M., Citarella, R., Efficient FEM-DBEM coupled approach for crack propagation simulations, Theoretical and Applied Fracture Mechanics, 91 (2017b) 76-85.

[17] Branco, R., Antunes, F.V., Costa, J.D., A review on 3D-FE adaptive remeshing techniques for crack growth modelling, Eng. Fract. Mech., 141 (2005) 170-195.

[18] Erdogan, F., Sih, G.C., On the extension of plates under plane loading and transverse shear, J Basic Engng 85D(4) (1963) 519–27.

[19] Sih, G.C. Strain energy density factor applied to mixed mode crack problems, Int J Fract., 10 (1974) 305-321.

.

[20] Sih, G.C., Cha, B.C.K., A fracture criterion for three-dimensional crack problems, Eng. Fract. Mech. 6(4) (1974) 699-723.

[21] Schöllmann, M., Richard, H.A., Kullmer, G. and Fulland, M., A new criterion for the prediction of crack development in multiacially loaded structures, Int. J. Fract:, 117(2002) 129-141.

[22] Dhondt, G., Application of the Finite Element Method to mixed-mode cyclic crack propagation calculations in specimens, Int. J. Fatigue 58(2014) 2-11.

[23] Ayatollahi, M.R., Saboori, B., Maximum tangential strain energy density criterion for general mixed mode I/II/III brittle fracture, Int. J. Dam. Mech., 24(2015) 263-278.

[24] Hussain, M.A., Pu, S.L., Underwood, J., Strain energy release rate for a crack under combined Mode I and Mode II, Fract. Anal. ASTM STP, 560 (1974) 2-28.

[25] Shlyannikov, V.N., Mixed-mode static and fatigue crack growth in central notched and compact tension shear specimens, ASTM Special Technical Publication 1359, (1999) 279-294.

[26] Shlyannikov, V.N.: Fatigue crack paths for inclined cracks and surface flaws under biaxial loading, Eng. Frac. Mech. 77(2010) 1772-1780.

[27] Shlyannikov, V.N.: T-stress for crack paths in test specimens subject to mixed mode loading, Eng. Frac. Mech. 108(2013) 3-18.

[28] Carpinteri, A., Ronchei, C., Vandadori, Sl, Stress intensity factors and fatigue growth of surface cracks in notched shells and round bars: two decades of research work, Fatigue Fract. Eng. Mater. Struct., 36(11) (2013) 1164-1177.

[29] Shlyannikov, V.N., Tumanov, A.V. and Zakharov, A.P.: The mixed mode crack growth rate in cruciform specimens subject to biaxial loading, Theor. Appl. Frac. Mech. 73(1014) 68-81.

[30] Shlyannikov, V.N., Tumanov, A.V., Zakharov, A.P. Gerasimenko, A.A., Surface flaws behavior under tension, bending and biaxial cyclic loading, Int. J. Fatigue, 92(2016) 557-576.

[31] Shlyannikov, V.N. and Zakharov, A.P.: Generalization of mixed mode crack behavior by the plastic stress intensity factor, Theor. Appl. Frac. Mech. 91(2017) 52-65 [32]A. Samir, A. Simon, A. Scholz and C. Berger: Service-type

creep-fatigue experiments with cruciform specimens and modelling of deformation, Int. J. Fatigue 28(2006) 643-651.

[32] Lepore, M., Berto, F., Kujawski, D., Non-linear models for assessing the fatigue crack behaviour under cyclic biaxial loading in a cruciform specimen, Theoretical and Applied Fracture Mechanics, 100 (2019) 14-26.

[33] Samir, A., Simon, A., Scholz, A., Berger, C., Service-type creep-fatigue experiments with cruciform specimens and modelling of deformation, Int. J. Fatigue 28(2006) 643-651.

[34] Cui, L., P. Wang, H. Hoche, A. Scholz, C. Berger: The influence of temperature transients on the lifetime of modern high-chromium rotor steel under service-type loading, Materials science and engineering A, 560 (2013), 767-780

[35] Dhondt, G., Rupp, M. and Hackenberg, H.-P., A modified crack propagation description, Eng. Frac. Mech. 146 (2015) 21-30.

[36] Downing, S.D., Socie, D.F., Simple rainflow couting algorithms, Int. J. Fatigue, 4(1982),31-40

[37] BEASY V10r14 (2011). Documentation. C.M. BEASY Ltd.

[38] Rigby, R.H., Aliabadi, M.H. Mixed-mode J-integral method for analysis of 3D fracture problems using BEM, Eng. Anal. Boundary Elem., 11 (1993) 239–256.

[39] Rigby, R.H. Aliabadi, M.H., Decomposition of the mixed-mode J-integral – revisited, Int. J. Solids Struct., 35(17) (1998) 2073–2099.

[40] Chambers, A.C., Hyde, T.H., Webster, J.J., Mixed mode fatiue crack growth at 550°C under plane stress conditions in jethete M152, Eng. Fract. Mech., 39 (1991) 603-619.

[41] Shi, X.Q., Zhang, X.R., Pang, J.H.L., Determination of interface fracture toughness of adhesive joint subjected to mixed-mode loading using finite element method, Int. J. Adhesion Adhes., 26(2006) 249-260.

[42] Mi, Y., Three dimensional dual boundary element analysis of crack growth, Ph.D. Thesis. University of Portsmouth, (1995) USA.

[43] Walker, K., The Effect of Stress Ratio During Crack Propagation and Fatigue for 2024-T3 and 7075-T6 Aluminum, American Society for Testing and Materials, (1970) ASTM STP 462.

[44] Lee, Y.M., Sim, J.M., Chang, Y.-S., Shin, I.-H., Yang, J.-S., PWSCC growth analyses by boundary element method considering weld residual stress distributinos, Int. J. Pres. Ves. Pip., 168 (2018) 156-165.